Elastocapillary network model of inhalation

Jean-François Louf [1,*] Felix Kratz [1,2,*] and Sujit S. Datta [1,†]

[1]*Department of Chemical and Biological Engineering, Princeton University, Princeton, New Jersey 08544, USA*

[2]*Department of Physics, Technical University of Dortmund, Dortmund 44227, Germany*

(Received 27 August 2020; accepted 8 November 2020; published 16 December 2020)

The seemingly simple process of inhalation relies on a complex interplay between muscular contraction in the thorax, elastocapillary interactions in individual lung branches, propagation of air between different connected branches, and overall air flow into the lungs. These processes occur over considerably different length and timescales; consequently, linking them to the biomechanical properties of the lungs, and quantifying how they together control the spatiotemporal features of inhalation, remains a challenge. We address this challenge by developing a computational model of the lungs as a hierarchical, branched network of connected liquid-lined flexible cylinders coupled to a viscoelastic thoracic cavity. Each branch opens at a rate and a pressure that is determined by input biomechanical parameters, enabling us to test the influence of changes in the mechanical properties of lung tissues and secretions on inhalation dynamics. By summing the dynamics of all the branches, we quantify the evolution of overall lung pressure and volume during inhalation, reproducing the shape of measured breathing curves. Using this model, we demonstrate how changes in lung muscle contraction, mucus viscosity, and surface tension, and airway wall stiffness—characteristic of many respiratory diseases, including those arising from COVID-19, cystic fibrosis, chronic obstructive pulmonary disease, asthma, and emphysema—drastically alter inhaled lung capacity and breathing duration. Our work, therefore, helps to identify the key factors that control breathing dynamics and provides a way to quantify how disease-induced changes in these factors lead to respiratory distress.

DOI: 10.1103/PhysRevResearch.2.043382

I. INTRODUCTION

The ongoing COVID-19 crisis highlights the critical importance of lung biomechanics in our everyday lives: COVID-19 patients frequently develop shortness of breath and often, debilitating and possibly fatal respiratory failure [1–5]. These complications are thought to arise in part from virus-induced alterations in the biomechanical properties of the lungs—specifically, an increase in the surface tension of the airway mucus lining and a decrease in the strength of the thoracic muscles [6,7]. Such complications also manifest in diverse other disorders arising from cystic fibrosis (CF), chronic obstructive pulmonary disease (COPD), asthma, and emphysema; these are again thought to be linked to changes in airway surface tension or muscular contraction as well as to other alterations in the mechanics of airway tissues and secretions, such as an increase in mucus viscosity and a decrease in airway wall stiffness [8–11]. As a result, treatments frequently rely on mechanical ventilation and exogenous administration of surfactant and/or mucus-thinning agents [4,12–23]. However, these interventions often proceed by trial and error due to a limited understanding of how biomechanical factors impact the overall dynamics of breathing.

Although experiments provide a wealth of information quantifying muscle strength, mucus surface tension and viscosity, and lung airway wall stiffness, directly connecting alterations in these tissue-scale biomechanical factors to organ-scale alterations in breathing is challenging. In particular, measurements of tissue properties can be invasive and often do not provide a way to assess the larger-scale impact of variations in these factors, whereas measurements of overall breathing dynamics are noninvasive but do not shed light on the underlying biomechanical factors at play. Computational models provide a promising way to overcome these limitations. For example, computational fluid dynamics approaches are capable of resolving air pressure and flow-induced stresses in the lungs with exquisite detail [24–37]; however, they are computationally intensive and frequently focus on static lung morphologies for simplicity. Conversely, sophisticated pulmonary mechanics models have been developed to elaborate the competition between capillary, viscous, and elastic stresses in determining how individual lung branches deform [38–51]; however, these models do not incorporate the complex hierarchical structure of the lungs and, thus, cannot reproduce the full dynamics of breathing. Models that simplify the representation of the different lung branches as an interconnected network provide a promising way to bridge these extremes; however, previous implementations have not treated dynamic changes in lung structure during breathing or

*These authors contributed equally.

†Author to whom correspondence should be addressed: ssdatta@princeton.edu

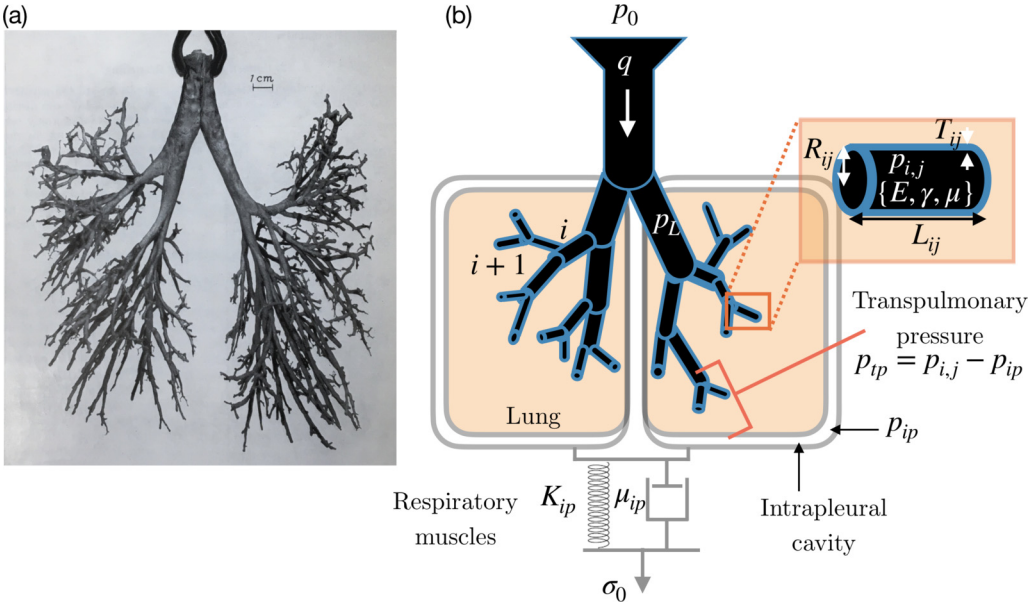

FIG. 1. (a) Cast of the bronchial tree of an adult human lung from Ref. [56]. (b) Schematic of our model of the lungs as a branched network of mucus-lined flexible thin-walled cylinders coupled to a viscoelastic thoracic cavity, represented by the spring and dashpot. Each branch opens at a rate and a pressure that is determined by input biomechanical parameters, enabling us to elucidate how the mechanical properties of lung tissues and secretions impact breathing dynamics.

have only been used to specifically investigate the influence of structural heterogeneity on breathing [52–55]. Thus, an understanding of how lung biomechanics impacts respiration in general remains elusive.

Here, we address this problem by developing a dynamic network model of the lungs that connects the multiscaled processes underlying inhalation: contraction of the thoracic muscles, opening of the individual lung branches, flow of the mucus lining, propagation of air between different connected branches, and overall air flow into the lungs. We hypothesize that the network representation of these processes resolves the relevant length and time scales, while still providing a simplified and computationally tractable representation of the interconnected and hierarchical geometry of the lungs. In support of this hypothesis, we show that our model can describe the evolution of overall lung pressure and volume as well as the hierarchical and heterogeneous openings of different lung branches, during inhalation starting from a completely closed respiratory zone as a proof of principle. We use the model to demonstrate how disease-induced weakening of the thoracic muscles, increased mucus viscosity and surface tension, and alterations in lung airway wall elasticity impact inhalation. Thus, our results help elucidate how lung biomechanics control breathing dynamics.

II. THEORY OF INHALATION DYNAMICS

A. Lung network representation

Motivated by morphological data, we computationally represent the lungs as a binary branched network of thin-walled liquid-lined flexible cylinders coupled to a viscoelastic thoracic cavity (Fig. 1). This tree can be classified into two sections leading from the trachea [57,58], indexed by the generation number i: the conducting zone ($0 \leqslant i \leqslant 16$), which has a constant open volume and does not contribute to oxygen uptake into the bloodstream, and the respiratory zone ($17 \leqslant i \leqslant 23$), which has branches that can collapse and open during respiration, and is the primary site of oxygen uptake. We, therefore, represent the conducting zone as one static airway branch and the respiratory zone as a binary tree spanning generations 17–23. We index each individual branch by the labels i and j, where $17 \leqslant i \leqslant 23$ denotes the generation number and $1 \leqslant j \leqslant 2^i$ corresponds to the index of the branch within a given generation i. The branches are all connected; thus, branches deeper in the lungs are only able to open when branches above them have opened.

Each branch is characterized by an open inner radius R_{ij}, length L_{ij}, and wall thickness T_{ij}, and, therefore, an open airway volume $V_{ij} = \pi R_{ij}^2 L_{ij}$ [Fig. 1(b), right inset]. For each generation, the mean values of these morphological parameters $R_i \equiv \langle R_{ij} \rangle_j = \sum_{j=1}^{2^i} R_{ij}/2^i$, $L_i \equiv \langle L_{ij} \rangle_j = \sum_{j=1}^{2^i} L_{ij}/2^i$, and $T_i \equiv \langle T_{ij} \rangle_j = \sum_{j=1}^{2^i} T_{ij}/2^i$ are given by experimental measurements of the mean branch radius, length, and thickness, respectively (Table I). To incorporate heterogeneity, a natural feature of the lungs, we then randomly select the individual R_{ij}, L_{ij}, and T_{ij} from a uniform distribution bounded by $\pm 25\%$ of R_i, L_i, and T_i, respectively. The results shown in Figs. 2–7 all utilize the same lung architecture parametrized by the same values of $\{R_{ij}, L_{ij}, T_{ij}\}$ to isolate the influence of biomechanical factors on breathing. However, an advantage of our network representation is that it is generalizable: Specific values of the morphological parameters can be incorporated in future extensions of this paper. For example, our model could be used to assess the distributions of outcomes across different airways with different $\{R_i, L_i, T_i\}$'s, or between different realizations of the same airways having the same $\{R_i, L_i, T_i\}$'s,

TABLE I. Morphological parameters used in our simulations, obtained from experimental measurements [56,59].

Generation i	Mean radius R_i (mm)	Mean length L_i (mm)	Mean wall thickness T_i (mm)
17	0.270	1.41	0.0236
18	0.250	1.17	0.0229
19	0.235	0.99	0.0226
20	0.225	0.83	0.0227
21	0.215	0.70	0.0228
22	0.205	0.59	0.0231
23	0.204	0.50	0.0250

given the importance of structural heterogeneity on breathing [55].

Furthermore, to incorporate the biomechanical properties of lung tissues, we make the simplifying assumption that the inner walls of the branches are uniformly coated by a Newtonian fluid of negligible thickness with dynamic shear viscosity μ and surface tension γ, and the lung airway wall is a linear elastic solid with Young's modulus E; we use values of μ, γ, and E obtained from experimental measurements as listed in Table II and take them to be constant throughout the lungs. This model, therefore, represents a key first step toward computationally describing the lungs, which in reality have non-Newtonian mucus with a non-negligible generation-dependent thickness as well as generation-dependent values of the parameters μ, γ, and E. However, our network representation enables specific branch-dependent values of these

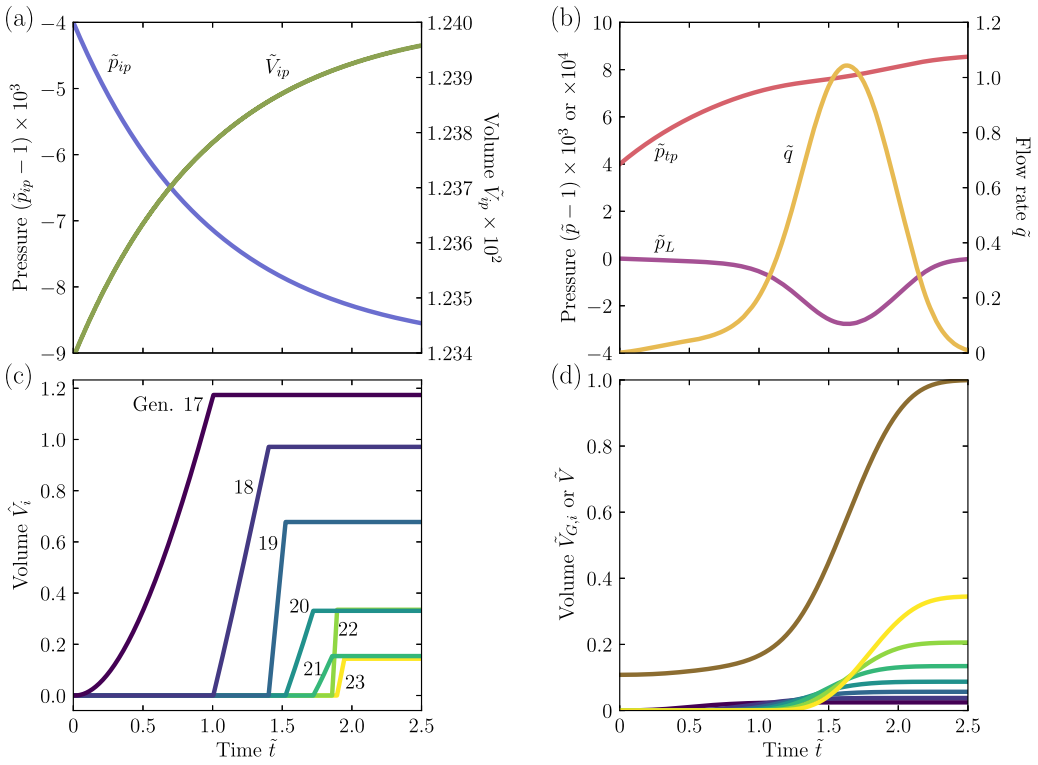

FIG. 2. Typical inhalation dynamics. Plots show the simulated evolution of lung pressures and volumes as a function of the dimensionless inhalation duration $\tilde{t} \equiv t/\tau_B$, where $\tau_B = 1$ s is the characteristic inhalation time. (a) Pressure p_{ip} (blue) and volume V_{ip} (green) of the intrapleural cavity, normalized by atmospheric pressure p_0 and the maximal lung volume V_0, respectively. To show the small variation of $\tilde{p}_{ip}$ and $\tilde{V}_{ip}$ more clearly, we plot $(\tilde{p}_{ip}-1)\times 10^3$ (left) and $\tilde{V}_{ip}\times 10^2$ (right). (b) Transpulmonary pressure p_{tp} (red), respiratory zone pressure p_L (purple), and air inflow rate q (yellow). Pressures are normalized by atmospheric pressure whereas flow rate is normalized by the characteristic flow rate V_0/τ_B. To show the small variation of the pressures more clearly, we plot $(\tilde{p}-1)\times 10^3$ in the case of $p = p_{tp}$ and $(\tilde{p}_L-1)\times 10^4$ in the case of $p = p_L$. (c) Open volumes of individual connected branches in each generation of the respiratory zone, normalized by the characteristic branch-scale volume $\pi R_{17}^2 L_{17}$, where R_{17} and L_{17} are the mean values of the branch radius and length at the first generation of the respiratory zone, respectively; different numbers by the curves indicate the generation number i. (d) Dark blue to yellow curves show the total open volume summed over each generation i, $V_{G,i}$ with the colors corresponding to the same generations as in panel (c). The brown curve shows the total open volume of airways of the lung V. Both $V_{G,i}$ and V are normalized by the maximal lung airway volume. In all these simulations, applied muscular stress $\sigma_0 = 500$ Pa, mucus viscosity $\mu = 100$ mPa s, mucus surface tension $\gamma = 15$ mN/m, and biomechanical parameter $\zeta = 1.3\times 10^{-3}$.

TABLE II. Biomechanical parameters used in our simulations, obtained from experimental measurements.

Biomechanical parameters	Value	Reference
Young's modulus of the lung airway wall E	5 kPa	[60,61]
Poisson's ratio of the airway wall ν	0.5	[62]
Mucus dynamic shear viscosity μ	100 mPa s	[63–65]
Applied muscular stress σ_0	500 Pa	[66–69]
Initial volume of the intrapleural cavity $V_{ip,0}$	20 mL	[70]
Maximal open airway volume V_0	1.675 L	[56]
Initial pressure of the intrapleural cavity $p_{ip,0}$	p_0-400 Pa	[71]
Effective bulk modulus of the intrapleural cavity K_{ip}	100 kPa	[60,61]
Mucus surface tension γ	15 mN/m	[72,73]

biomechanical parameters to be incorporated, which would be another useful direction for future work.

B. Stress exerted by thoracic muscles

As a first step toward modeling the full dynamics of respiration, here we consider the process of inhalation starting from a completely closed respiratory zone—characteristic of newborn infants or patients with severe respiratory distress [74]. We, therefore, initialize the model with all branches with $17 \leqslant i \leqslant 23$ closed. Building on this model to explore the additional dynamics of exhalation as well as multiple breathing cycles will be an important direction for future research.

Inhalation begins with the contraction of the thoracic muscles that as a first approximation we assume pull with a constant stress σ_0 on the intrapleural cavity. Motivated by previous work [61,75], we model the viscoelastic behavior of the chest using a Kelvin-Voigt model, which treats the chest as a combination of an elastic spring and a viscous dashpot connected in parallel [Fig. 1(b), bottom]: $\sigma(t) \equiv \sigma_0 = K_{ip}\varepsilon(t) + \mu_{ip}\dot{\varepsilon}(t)$, where K_{ip} and μ_{ip} are the effective elastic and viscous constants characterizing the intrapleural cavity and $\varepsilon \equiv \Delta V_{ip}(t)/V_{ip,0}$ represents the volumetric strain in the intrapleural cavity, where ΔV_{ip} represents the difference in the cavity volume compared to its initial value $V_{ip,0}$. Thus, the intrapleural space expands over time in a stress-dependent manner,

$$\varepsilon(t) = \varepsilon_{max}(1 - e^{-t/\tau_B}), \tag{1}$$

where $\varepsilon_{max} \equiv \sigma_0/K_{ip}$ is the maximal strain and $\tau_B \equiv \mu_{ip}/K_{ip}$ is the characteristic timescale of inhalation. Based on previous measurements [60,61], we take $K_{ip} = 100$ kPa and $\tau_B = 1$ s.

C. Elastocapillary interactions in individual branches

The expansion of the thoracic cavity reduces the intrapleural pressure p_{ip} (Fig. 1, right): given a fixed amount of air within the intrapleural space, $p_{ip}(t) = p_{ip,0}/[1 + \varepsilon(t)]$, where $p_{ip,0} \approx 99.6$ kPa as determined experimentally [76] and $\varepsilon(t)$ is given by Eq. (1). Thus, the transpulmonary pressure difference across the lung airway wall $p_{tp}(t) \equiv p_L(t) - p_{ip}(t)$ transiently increases; here $p_L(t)$ is the air pressure in the respiratory zone, which we take to be constant throughout due to the low air flow resistance of the respiratory zone, as justified in the *Methods*.

As established in many previous studies [55,77–79], as p_{tp} increases, it exceeds the threshold pressure $p_{ij}^{th} = 8\gamma/R_{ij}$ required to open a collapsed branch ij that is in contact with the open region of the lungs [38]. In this case, an air finger propagates into the branch at a speed U_{ij} that is determined by a complex interplay between viscous forces in the airway mucus lining as the branch is pulled apart, capillary forces holding the walls of the branch together, and elastic forces resisting bending of the branch walls. Motivated by the results of previous three-dimensional numerical solutions [38], we estimate this speed using the relation $\mathrm{Ca}_{ij} = \frac{1}{\Gamma_{ij}}\frac{p_{tp}-p_{ij}^{th}}{\gamma/R_{ij}}$ where $\mathrm{Ca}_{ij} \equiv \mu U_{ij}/\gamma$ is the capillary number and $\Gamma_{ij} \equiv (\gamma/R_{ij})/B_{ij}$ is a dimensionless parameter that quantifies the competition between capillary and elastic stresses in the branch with bending stiffness $B_{ij} \equiv E(T_{ij}/R_{ij})^3/12(1-\nu^2)$ and $\nu \approx 0.5$ is the Poisson's ratio of the airway wall. This equation highlights three key features of branch opening. First, capillary forces hold the walls of a branch together, and, thus, the transpulmonary pressure p_{tp} must overcome the capillary pressure threshold p_{ij}^{th} to force a branch to open. Second, the elastic energy penalty associated with deforming a branch also promotes opening as quantified by Γ_{ij}. Third, branch opening is not instantaneous, but is limited by viscous dissipation as the mucus lining is pushed apart as quantified by Ca_{ij}.

We directly implement this relation into our model with the condition that a given branch can only open if its proximal end is in contact with the open region of the lungs. For ease of computation we treat the branch as being split into a fully open fraction with time-dependent volume $V_{ij}(t)$ and a remaining fully closed fraction. In nondimensional form, this relation can then be expressed as

$$\frac{\partial \hat{V}_{ij}}{\partial \hat{t}} = \frac{\zeta \hat{R}_{ij}^3}{\hat{\Gamma}_{ij}}\left[\hat{p}_{tp}(\hat{t}) - \hat{p}_{ij}^{th}\right], \tag{2}$$

where the hat notation $\hat{()}$ indicates that the variables V_{ij}, t, R_{ij}, Γ_{ij}, and $p_{tp} - p_{ij}^{th}$ have been normalized by the characteristic branch-scale quantities $\pi R_{17}^2 L_{17}$, μ/p_{17}^{th}, R_{17}, $(\gamma/R_{17})/B_{17}$, and p_{17}^{th}, respectively, where the subscript 17 refers to the mean value at the first generation of the respiratory zone. This nondimensional form reveals that the biomechanical parameter $\zeta \equiv (R_{17}/L_{17})/\Gamma_{17}$ is a key factor that governs the amount of lung opening during inhalation: When ζ is large, elasticity tends to peel the lung branches open, whereas when ζ is small, capillarity tends to hold lung branches shut.

D. Overall opening of the lungs

The physics described in the previous subsection governs the opening of individual branches; summing over all open regions of the airways then yields the total opened lung volume $V(t) = V_C + V_R(t) = V_C + \sum_{i=17}^{23} \sum_{j=1}^{2^i} V_{ij}(t)$, where V_C is the constant open volume of the conducting zone and V_R is the time-dependent open volume of the respiratory zone with V_{ij} given by Eq. (2). Thus, as p_{tp} increases, the open volume of the respiratory zone V_R increases, causing the lung pressure p_L to transiently decrease. This decrease in pressure draws air into the lungs from the atmosphere with a volumetric flow rate of magnitude $q(t) \sim [p_0 - p_L(t)]/\sum_{i=0}^{16} \left(\sum_{j=1}^{2^i} \Omega_{ij}^{-1}\right)^{-1}$ through the conducting zone (*Methods*), where $p_0 \approx 101$ kPa is atmospheric pressure.

E. Computational implementation of the model

Analysis of these coupled processes enables us to quantitatively model the full dynamics of inhalation. Specifically, as detailed in the *Methods*, we input values of the morphological parameters $\{R_{ij}, L_{ij}, T_{ij}\}$ and the biomechanical parameters $\{\mu, \gamma, E, \sigma_0\}$ and iteratively solve the equations described in the *Theory* section at uniform discrete time-steps Δt. This scheme, thus, enables us to determine the full evolution of the pressures $\{\tilde{p}_{ip}, \tilde{p}_{tp}, \tilde{p}_L\}$, the volumes $\{\tilde{V}_{ip}, \hat{V}_{ij}, \tilde{V}\}$ and the flow rate $\tilde{q}$ over time $\tilde{t}$, where the tilde notation (˜) indicates lung-scale variables that have been normalized by the atmospheric pressure p_0, maximal open lung volume V_0, characteristic flow rate V_0/τ_B, and breathing time τ_B, respectively. Importantly, this network representation reduces computational cost: The complete dynamics of inhalation can be obtained within a matter of minutes on a conventional personal computer. For example, the entirety of the results in Fig. 2 were obtained using a laptop with an 8th Generation Intel Core i7-8750H 6 core processor with 2.2 GHz and 16 GB RAM in 20 min. Thus, our network model provides a computationally tractable way to characterize the dynamics of respiration that can be implemented by specialists and general users alike.

III. RESULTS

A. Typical inhalation dynamics

We begin by describing the full inhalation dynamics of a representative healthy lung, using published measurements for the input parameters [56,60,61,63–68,70–73]. The simulation captures the expected dynamics of inhalation. First, the contraction of the respiratory muscles generates a stress on the intrapleural cavity, expanding it [Fig. 2(a), green] and reducing its internal pressure [Fig. 2(a), blue]. The transpulmonary pressure difference between the lung interior and the intrapleural space, subsequently, builds up [Fig. 2(b), red], causing respiratory branches to successively open [Figs. 2(c)and 2(d), dark blue to green to yellow], reducing the pressure in the respiratory zone [Fig. 2(b), purple] and driving air flow into the lungs [Fig. 2(b), yellow]. This process continues as the intrapleural cavity expands over time. Eventually, however, the applied stress is able to expand the chest by less and less [Fig. 2(a), plateau in green curve], and branches open at a slower rate; the flow rate of air into the lungs eventually reaches zero at a time $\tilde{t}_{max} \approx 2.5$ [Fig. 2(b), yellow], and inhalation ceases.

Each generation is made of progressively smaller branches having progressively larger threshold pressures for opening. Thus, we expect lung opening to be hierarchical: The larger proximal branches open first, and then smaller distal branches open later, after air is able to propagate to them and exceed the capillary pressure threshold. Our computational model captures this hierarchy of branch opening as shown in Figs. 2(c) and 2(d), complementing previous investigations of collective branch opening [55,77–79]. Figure 2(c) shows an example of individual connected branches in different generations as they open. The branch in the first generation of the respiratory zone opens first ($i = 17$, dark blue); once it has fully opened, air can propagate into the branch in the next generation ($i = 18$, lighter blue), causing successive opening of branches through the different generations and eventually reaching the terminal alveoli ($i = 23$, yellow). Notably, however, even though these terminal generations must open later, and although their individual branches are smaller, they collectively contribute the largest volume to the open lung as shown in Fig. 2(d); the dark blue to yellow curves show the volume of all the open branches in a given generation i, $V_{G,i}(t) = \sum_{j=1}^{2^i} V_{ij}(t)$, whereas the brown curve shows the total open volume of the lung $V(t)$. Although the first generation of the respiratory zone (dark blue) is the first to open during inhalation, it contributes only $\sim 3\%$ volume to the open lung; by contrast, the terminal generation (yellow) is the last to open, but contributes $\sim 35\%$ of the overall lung volume. Thus, our model quantifies the expectation that opening later generations is key for healthy lung performance.

B. Influence of changes in biomechanical parameters on inhalation

Having characterized the typical dynamics of inhalation, we next investigate how these dynamics are controlled by key biomechanical factors. Specifically, motivated by their relevance to respiratory distress stemming from the ongoing COVID-19 crisis as well as from prevalent conditions, such as CF, COPD, asthma, and emphysema, we focus on the role of four key factors: (i) muscle-induced stress σ_0, (ii) mucus viscosity μ, (iii) mucus surface tension γ, and (iv) airway wall stiffness E.

C. Role of muscle-induced stress

Patients with COVID-19, CF, or COPD frequently exhibit fatigue and muscle weakness [80,81]; similar symptoms also manifest in patients who have undergone mechanical ventilation as a treatment for prolonged periods of time [82]. The analysis presented in the *Theory* section suggests that this decrease in σ_0 reduces the expansion of the intrapleural cavity during inhalation, limiting the amount of air that can be taken into the lungs and giving rise to respiratory distress.

Our simulations with varying σ_0 confirm this expectation. In particular, we find that the dynamics of lung opening strongly depend on the applied stress [Fig. 3(a)], indicating that it is a key regulator of breathing; reducing the stress exerted by the thoracic muscles decreases the rate at which

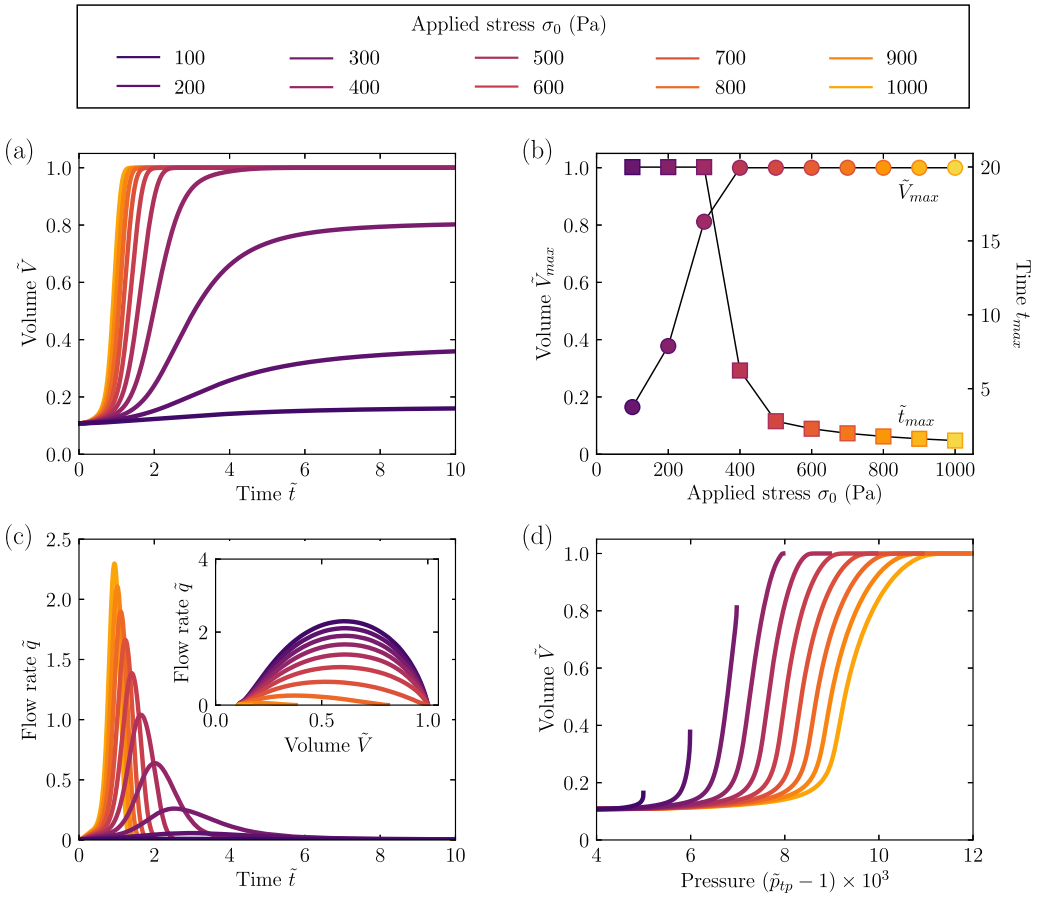

FIG. 3. Stress applied by thoracic muscles strongly regulates dynamics and full extent of inhalation. In all panels, different colors show different applied stresses σ_0. (a) Simulated evolution of the total open volume of the lung airways V, normalized by the maximal lung volume V_0 as a function of the dimensionless inhalation duration $\tilde{t} \equiv t/\tau_B$, where $\tau_B = 1$ s is the characteristic inhalation time. (b) Maximal opened volume of the lung airways V_{max} (circles) decreases, and the time needed to reach this volume t_{max} (squares) increases with decreasing applied stress. Volume and time are normalized by the maximal lung volume V_0 and the characteristic inhalation time τ_B, respectively. Simulations are performed for times up to $\tilde{t} = 20$; therefore, values of $\tilde{t}_{max}$ and $\tilde{V}_{max}$ for $\sigma_0 \leqslant 300$ Pa are truncated and could be even larger for simulations run over longer durations. (c) Air inflow rate q, normalized by the characteristic flow rate V_0/τ_B, over time. The inset shows the variation of the flow rate with total opened lung volume as is often measured experimentally via spirometry. (d) Opened lung volume V and transpulmonary pressure p_{tp} curves as is often measured experimentally. Pressure is normalized by atmospheric pressure p_0; to show the small variation of $\tilde{p}_{tp}$ more clearly, we plot $(\tilde{p}_{tp} - 1) \times 10^3$ on the horizontal axis. In all these simulations, mucus viscosity $\mu = 100$ mPa s, mucus surface tension $\gamma = 15$ mN/m, and biomechanical parameter $\zeta = 1.3 \times 10^{-3}$.

air is drawn in and prolongs the overall duration of inhalation [Fig. 3(c)]. Indeed, when σ_0 is reduced from its typical healthy value $\approx 500 - 2000$ Pa [66–69] as in the case of COPD ($\sigma_0 \approx 200$ Pa [68,69]), the full duration of lung opening takes nearly ten times longer and only reaches half the fully opened volume as shown by the squares and circles in Fig. 3(b), respectively. The corresponding stress-dependent pressure-volume [Fig. 3(d)] and flow rate-volume [Fig. 3(c), inset] curves obtained in our simulations are strikingly similar to those observed in experimental measurements [83]. Thus, our computational approach provides a way to quantify the impact of specific changes in muscle-induced stress on inhalation, shedding light on its relative influence in causing respiratory distress.

D. Role of mucus viscosity

A common symptom of bronchitis, CF, COPD, interstitial lung disease, and possibly COVID-19 is a large increase in the viscosity of lung mucus [64,84–87]. The analysis presented in the *Theory* section suggests that this increase in μ increases the timescale over which individual lung branches open, possibly slowing the opening dynamics during inhalation and giving rise to respiratory distress.

Our simulations with varying μ confirm this expectation. In particular, we find that the dynamics of lung opening strongly depend on the mucus viscosity [Fig. 4(a)], indicating that it is another key regulator of breathing; increasing the mucus viscosity increases the time needed to reach the capillary pressure threshold p^{th} and open airway branches, decreasing the rate at which air is drawn in and prolonging the overall duration of inhalation [Fig. 4(c)]. Indeed, when μ is increased by a factor of $\sim$10 from its typical healthy value of $\approx$100 mPa s as can be the case in many lung diseases [64,84–87], the fully opened lung volume is unchanged, but the full duration of lung opening takes approximately five times longer as shown by the circles and squares in Fig. 4(b), respectively.

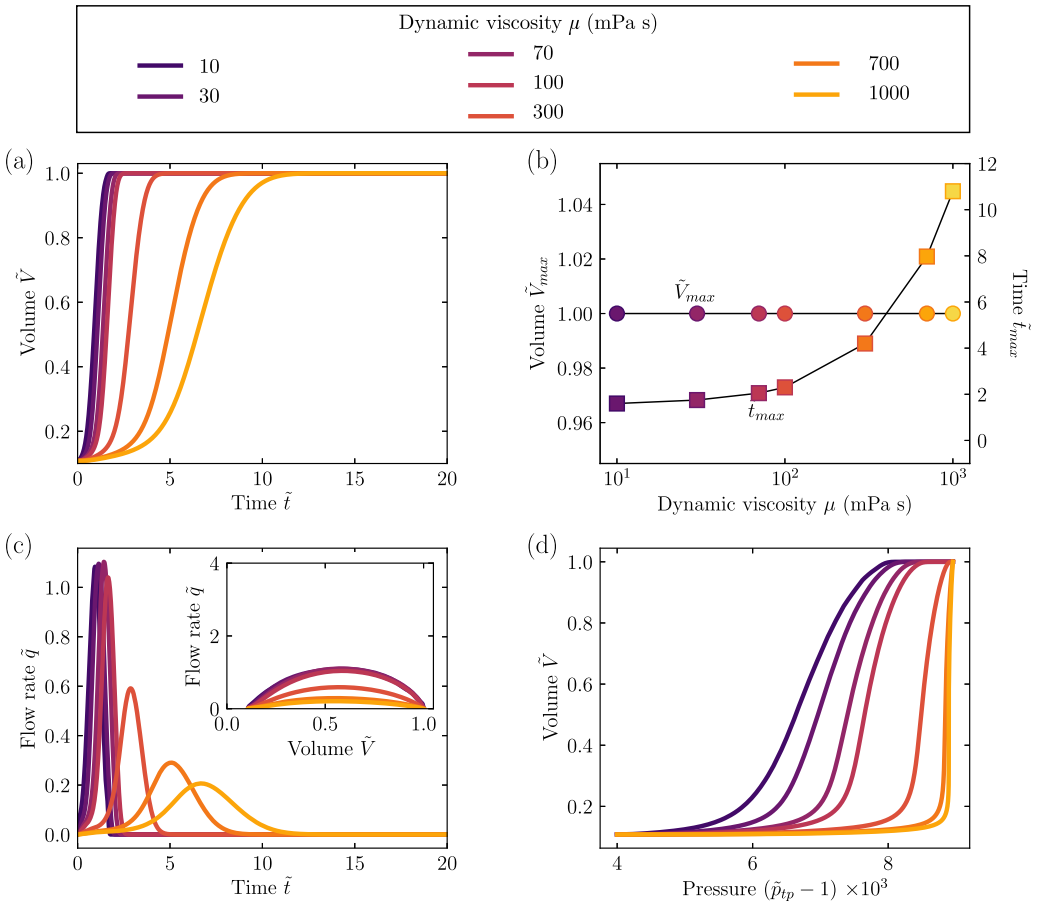

FIG. 4. Mucus viscosity strongly regulates inhalation dynamics. In all panels, different colors show different surface tensions μ. (a) Simulated evolution of the total open volume of the lung airways V, normalized by the maximal lung volume V_0 as a function of the dimensionless inhalation duration $\tilde{t} \equiv t/\tau_B$, where $\tau_B = 1$ s is the characteristic inhalation time. (b) Maximal opened volume of the lung airways V_{max} (circles) is constant, but the time needed to reach this volume t_{max} (squares) increases with increasing viscosity: mucus viscosity acts as a time-scaling parameter. Volume and time are normalized by the maximal lung volume V_0 and the characteristic inhalation time τ_B, respectively. (c) Air inflow rate q, normalized by the characteristic flow rate V_0/τ_B, over time. The inset shows the variation of the flow rate with total opened lung volume as is often measured experimentally via spirometry. (d) Opened lung volume V and transpulmonary pressure p_{tp} curves as is often measured experimentally. Pressure is normalized by atmospheric pressure p_0; to show the small variation of $\tilde{p}_{tp}$ more clearly, we plot $(\tilde{p}_{tp} - 1) \times 10^3$ on the horizontal axis. In all these simulations, applied muscular stress $\sigma_0 = 500$ Pa, mucus surface tension $\gamma = 15$ mN/m, and biomechanical parameter $\zeta = 1.3 \times 10^{-3}$.

Thus, alterations in mucus viscosity alter the dynamics but not the full extent of lung opening during inhalation. The corresponding viscosity-dependent pressure-volume [Fig. 4(d)] and flow rate-volume [Fig. 4(c), inset] curves obtained in our simulations are again strikingly similar to those observed in experimental measurements [83]. Thus, our computational approach provides a way to quantify the impact of specific changes in mucus viscosity on inhalation, shedding light on its relative influence in causing respiratory distress.

E. Role of mucus surface tension

One of the most prominent pathological features of COVID-19 is hindered production of lung surfactant due to viral infection, resulting in a large increase in the surface tension of airway mucus [88–91]. Similar complications arise in COPD and possibly in asthma and emphysema [81,92,93]. The analysis presented in the *Theory* section suggests that this increase in γ has two key effects both of which could contribute to respiratory distress. First, it increases the threshold pressure $p_{ij}^{th} = 8\gamma/R_{ij}$ required to open a collapsed branch ij. Second, it decreases the biomechanical parameter $\zeta \propto 1/\gamma$, which quantifies the competition between elastic and capillary stresses in the lung: when ζ is smaller, capillary forces are more likely to overcome the elastic energy penalty of holding lung branches shut. Both effects likely hinder the opening of the lungs during respiration, giving rise to respiratory distress in diseased patients.

Our simulations with varying γ confirm this expectation. In particular, we find that the dynamics of lung opening strongly depend on the surface tension [Fig. 5(a)], indicating that it is another key regulator of breathing; increasing the surface tension decreases the rate at which air is drawn in and prolongs the overall duration of inhalation [Fig. 5(c)]. Indeed, when γ is increased by just a factor of 2 from its typical healthy value $\approx$15 mN/m [72,73] as can be the case in COVID-19 and COPD [81,88–93], the full duration of lung opening takes nearly four times longer and only reaches a tenth of the

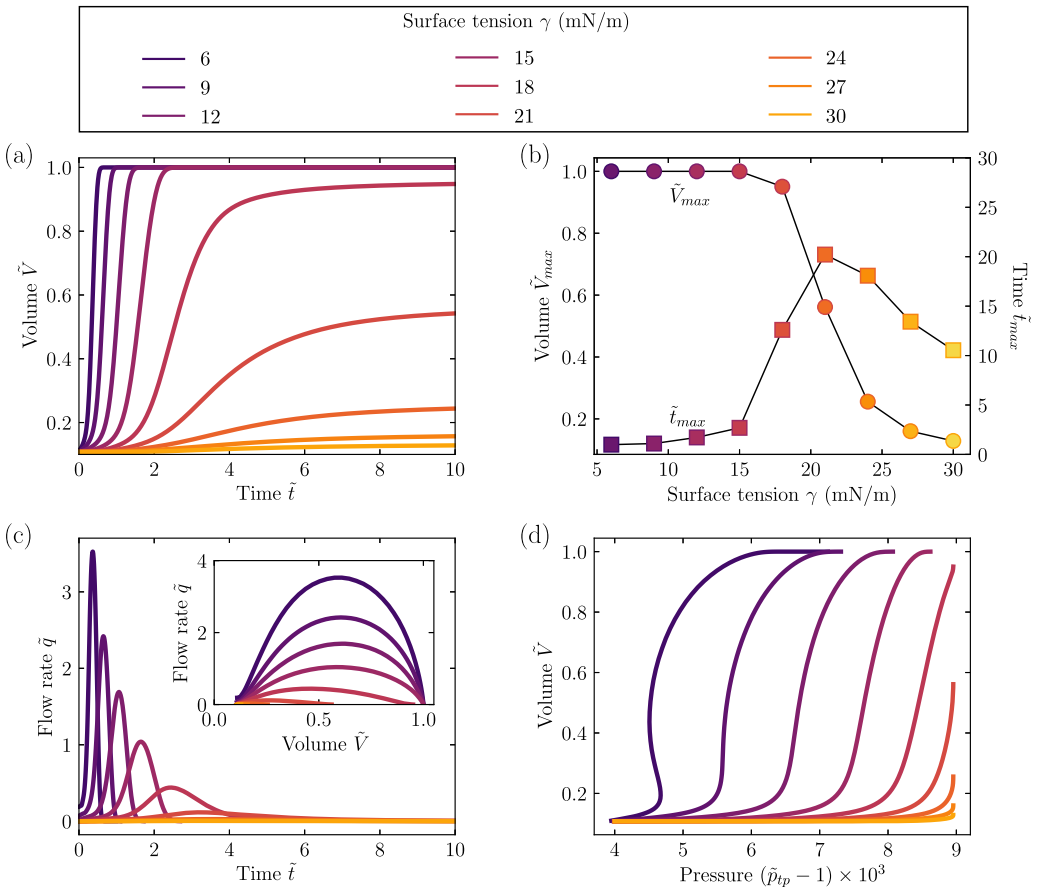

FIG. 5. Mucus surface tension strongly regulates full extent and dynamics of inhalation. In all panels, different colors show different surface tensions γ. (a) Simulated evolution of the total open volume of the lung airways V, normalized by the maximal lung volume V_0 as a function of the dimensionless inhalation duration $\tilde{t} \equiv t/\tau_B$, where $\tau_B = 1$ s is the characteristic inhalation time. (b) Maximal opened volume of the lung airways V_{max} (circles) decreases, and the time needed to reach this volume t_{max} (squares) increases and then decreases with increasing surface tension. Volume and time are normalized by the maximal lung volume V_0 and the characteristic inhalation time τ_B, respectively. (c) Air inflow rate q, normalized by the characteristic flow rate V_0/τ_B, over time. The inset shows the variation of the flow rate with total opened lung volume as is often measured experimentally via spirometry. (d) Opened lung volume V and transpulmonary pressure p_{tp} curves as is often measured experimentally. Pressure is normalized by atmospheric pressure p_0; to show the small variation of $\tilde{p}_{tp}$ more clearly, we plot $(\tilde{p}_{tp} - 1) \times 10^3$ on the horizontal axis. In all these simulations, applied muscular stress $\sigma_0 = 500$ Pa, mucus viscosity $\mu = 100$ mPa s, and biomechanical parameter $\zeta = 1.3 \times 10^{-3}$.

fully opened volume as shown by the squares and circles in Fig. 5(b), respectively. Intriguingly, the duration of inhalation varies nonmonotically with γ as shown by the squares: When γ is small, the capillary pressure threshold p^{th} is easily overcome, and the lungs open quickly, whereas as γ increases, capillarity increasingly resists lung opening, and the duration of inhalation increases. However, as γ increases above $\approx$ 21 mN/m, capillarity holds increasing numbers of branches of the lungs shut, and inhalation is truncated—causing the duration of inhalation to decrease again. This critical value of surface tension, above which lung airways stay closed, emerges naturally from our model. As shown in Fig. 2(d), the last airway generation is the largest contributor to the open lung volume, making up a third of the total lung volume. This generation is made of the smallest airway channels, which have the highest capillary pressure threshold to overcome before they can be opened. As a result, for this generation to open, the transpulmonary pressure P_{tp} needs to be greater than the threshold pressure $P_{23}^{th} = \frac{8\gamma_c}{R_{23}}$. By definition, $P_{tp} = P_L - P_{ip}$ with $P_{ip} = P_{ip,0}/[1 + \varepsilon(t)]$. Using the characteristic values $P_L \sim P_0$ and $\varepsilon(t) \sim \varepsilon_{max} = 5 \times 10^{-3}$ yields a maximal value for $P_{tp} \sim 900$ Pa. Combining this value with the mean radius of the airways in the last generation $R_{23} = 0.204$ mm yields a characteristic critical value of the surface tension, $\gamma_c \sim 22$ mN/m, in excellent agreement with our simulations.

This behavior also manifests in the simulated pressure-volume [Fig. 5(d)] and flow rate-volume [Fig. 5(c), inset] curves, which are again strikingly similar to those observed in experimental measurements [83]. Indeed, we even observe the previously reported [94,95] nonmonotonic variation of p_{tp} with V at low γ as shown by the dark purple curve: under these conditions, because the capillary pressure threshold p^{th} is easily overcome, rapid lung opening causes an abrupt decrease in the lung pressure—a phenomenon that has been termed an "elastic shock" [94,95]. Together, these results indicate that our computational approach provides a way to

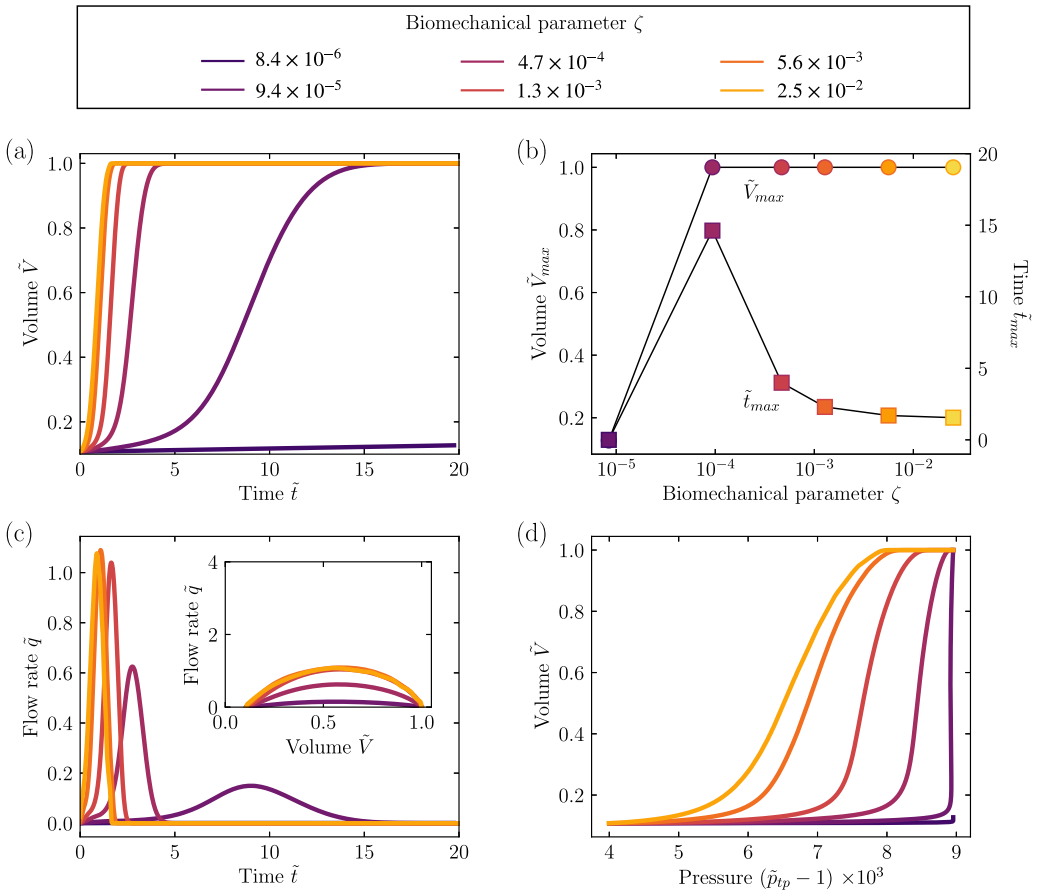

FIG. 6. Competition between elasticity and capillarity, quantified by the biomechanical parameter ζ, strongly regulates full extent and dynamics of inhalation. In all panels, different colors show different ζ. (a) Simulated evolution of the total open volume of the lung airways V, normalized by the maximal lung volume V_0, as a function of the dimensionless inhalation duration $\tilde{t} \equiv t/\tau_B$, where $\tau_B = 1$ s is the characteristic inhalation time. (b) Maximal opened volume of the lung airways V_{max} (circles) decreases, and the time needed to reach this volume t_{max} (squares) increases and then decreases, with increasing ζ. Volume and time are normalized by the maximal lung volume V_0 and the characteristic inhalation time τ_B, respectively. (c) Air inflow rate q, normalized by the characteristic flow rate V_0/τ_B over time. The inset shows the variation of the flow rate with total opened lung volume as is often measured experimentally via spirometry. (d) Opened lung volume V and transpulmonary pressure p_{tp} curves as is often measured experimentally. Pressure is normalized by atmospheric pressure p_0; to show the small variation of $\tilde{p}_{tp}$ more clearly, we plot $(\tilde{p}_{tp} - 1) \times 10^3$ on the horizontal axis. In all these simulations, applied muscular stress $\sigma_0 = 500$ Pa, mucus viscosity $\mu = 100$ mPa s, and mucus surface tension $\gamma = 15$ mN/m.

quantify the impact of specific changes in mucus surface tension on inhalation, isolating its relative influence in causing respiratory distress.

F. Role of airway wall stiffness

The elasticity of the airway wall changes greatly in disease, often in opposing ways. For example, buildup of excess fibrous connective tissue stiffens the airway walls in CF, COPD, and asthma [96–99], whereas weakening of the tissue leads to weaker airway walls in emphysema [11,100–102]; whether lung tissue elasticity increases, decreases, or stays unchanged is currently still being studied for COVID-19. The analysis presented in the *Theory* section suggests that weakening of the airway walls in emphysema hinders lung opening during inhalation and is likely the main contributor to respiratory distress in this case: Capillary forces due to the surface tension of the mucus lining tend to hold the soft walls of closed branches together. Conversely, we expect that stiffening of the airway walls in CF, COPD, and asthma paradoxically promotes lung opening, in opposition to the respiratory distress associated with these conditions: Stiffer lungs are more difficult to bend and close shut. Thus, in these cases, we expect that respiratory distress arises instead due to changes in other biomechanical factors, such as mucus viscosity and surface tension as suggested by clinical studies [103–105].

This competition between lung elasticity and capillarity is quantified by the biomechanical parameter $\zeta \equiv \frac{R_{17}}{L_{17}} \frac{E(T_{17}/R_{17})^3}{12(1-\nu^2)(\gamma/R_{17})}$. When ζ is large, elastic stresses, as quantified by the characteristic bending stiffness $B_{17} \equiv E(T_{17}/R_{17})^3/12(1-\nu^2)$, dominate and peel the lung branches open; conversely, when ζ is small, capillarity, as quantified by the characteristic capillary pressure γ/R_{17} dominates and tends to hold the lung branches shut. Our simulations with varying ζ, exploring the full physiological range of ζ using measurements of the variation that arises in E and γ [56,60,61,63,64,72,73], confirm this expectation. Similar to

the cases of varying σ_0 and γ, the dynamics of lung opening strongly depend on ζ [Fig. 6(a)], indicating that it is another key regulator of breathing; decreasing ζ decreases the rate at which air is drawn in and prolongs the overall duration of inhalation [Fig. 6(c)]. Intriguingly, similar to the case of γ, the duration of inhalation varies nonmonotically with ζ as shown by the squares in Fig. 6(b): When ζ is large, the lungs open quickly due to elastic stresses, whereas as ζ decreases, elastic stresses do not pull the lungs open as quickly, and the duration of inhalation increases. However, as ζ decreases below $\approx 10^{-4}$, elastic stresses cannot open many branches of the lungs, and inhalation is again truncated. This behavior also manifests in the simulated pressure-volume [Fig. 6(d)] and flow rate-volume [Fig. 6(c), inset] curves, which are again strikingly similar to those observed in experimental measurements [106,107].

We expect that because E decreases in emphysema [11,100–102], and γ possibly increases [81,92,93], ζ concurrently decreases and is, thus, the key biomechanical parameter that controls the onset of respiratory distress in this case. Conversely, because E increases in CF, COPD, and asthma [96–99], ζ may not decrease in these cases—suggesting that the onset of respiratory distress is instead controlled by increases in the mucus viscosity or surface tension as described above. Thus, our computational approach provides a way to separately quantify the impact of specific changes in airway wall stiffness E on breathing, shedding light on its relative influence in causing respiratory distress.

IV. DISCUSSION

The work described here represents a first step toward developing a model of the lungs that accurately describes the multiscaled spatial and temporal features of respiration, whereas still managing to be computationally tractable. Our dynamic network approach explicitly resolves the relevant length and timescales of branch opening during inhalation, while also capturing how opening propagates through the interconnected and hierarchical architecture of the lungs. We demonstrate this principle by directly connecting alterations in four key biomechanical factors—the strength of thoracic muscle contraction, the viscosity, surface tension of the airway mucus lining, and the elasticity of the airway wall—to overall alterations in breathing, in qualitative agreement with experimental and clinical findings. Our model, thus, helps to establish how lung biomechanics impact respiration—both deepening our fundamental understanding of this ubiquitous process and helping to elucidate how disease-induced changes in tissue-scale factors give rise to respiratory distress. However, despite the similarity between our results and published measurements, direct validation against systematic experimental measurements or more sophisticated models for which the values of all the input parameters are known will be a crucial next step.

Given the increasing prevalence of respiratory diseases [108], there is a critical need for computational tools capable of quantitatively assessing the efficacy of different therapeutic interventions, such as mechanical ventilation, exogenous administration of lung surfactant, and exogenous administration of mucus thinners. The work described here addresses this critical need. Specifically, it yields a generally applicable computational model for which measured treatment-induced changes in biomechanical parameters—e.g., $\{\sigma_0, \gamma, \zeta, \mu, K_{ip}\}$—can be input, and the impact on breathing outcome can be assessed. Because different treatments alter lung biomechanics in different ways, this approach may yield useful insights into how treatments that influence these specific parameters will affect breathing dynamics in general—and may eventually provide a straightforward way to quickly assess the impact of different treatments for a given patient.

The model presented here focused on the case of inhalation starting from a completely closed respiratory zone as a proof of principle; however, the dynamics described in the *Theory* section can be extended in future work to also describe the closure of individual lung branches due to compression of the thoracic cavity as well as breathing dynamics in a lung with regional atelectasis, involving a mixture of both open, partially closed, and fully closed branches. Accomplishing this extension will require development of a form of Eq. (2) that characterizes branch closure instead of opening, coupled with a variation of our inhalation model taking into account trapped air pockets. In this scenario, when the air finger responsible for opening reaches a trapped air pocket downstream, the open region connected to the open proximal (upstream) end of the lungs will abruptly increase in size. The distal end of the trapped air pocket will then be the new leading edge of branch opening, thereby decreasing the overall duration of inhalation. Furthermore, while our model of the dynamics of airway opening [given by Eq. (2)] is based on previous three-dimensional numerical solutions of air finger propagation into a completely closed branch, we note that the presence of trapped air may change these dynamics. Indeed, as suggested by Heap and Juel [109], the shape of the air finger can be modified in this case, leading to faster branch reopening. This process will likely also reduce the total volume of air inhaled. For example, Fig. 2(d) shows the total lung volume as a function of time during inhalation starting with a fully closed lung. If trapped air is initially present, the initial open lung volume will be bigger, but the maximal lung volume at the end of inhalation will be minimally altered, resulting in a reduced total volume of air inhaled. Furthermore, for both inhalation and exhalation, Eq. (2) can be replaced by the results of more sophisticated tube models that incorporate nonaxisymmetric deformation modes, possible collapse of the mucus film, mucus-wall liquid-solid interactions arising from the competition among viscous stress, capillary stresses, and wall deformations, and heterogeneities in airway branch geometry [38–45,47–51,57,110–112]. Finally, although our network representation necessarily simplifies many of the rich complexities of the lung in favor of ease of computation, it can be extended by incorporating different lung architectures by directly inputting specific values of $\{R_{ij}, L_{ij}, T_{ij}\}$; heterogeneity in the biomechanical parameter values by directly inputting specific values of $\{E_{ij}, \gamma_{ij}, \mu_{ij}\}$; and non-Newtonian mucus rheology by incorporating a rate-dependent viscosity in Eq. (2). Exploring the influence of these different features on breathing will be an important extension of our paper.

V. METHODS

To simulate the dynamics of inhalation, we implement the rules given in the *Theory* section in discretized form, evaluating volumes, pressures, and flow rates at successive time steps separated by $\Delta\tilde{t}$ using the iterative scheme described below. We use two different notations to differentiate between branch-scale quantities and overall lung-scale quantities. The tilde notation ($\tilde{}$) indicates that pressure, volume, flow rate, time, and flow resistance have been normalized by the atmospheric pressure p_0, maximal open lung volume V_0, characteristic flow rate V_0/τ_B, breathing time τ_B, and characteristic flow resistance $p_0\tau_B/V_0$, respectively. The hat notation ($\hat{}$) indicates that the variables V_{ij}, t, R_{ij}, Γ_{ij}, and $p_{tp} - p_{ij}^{th}$ have been normalized by the characteristic branch-scale quantities $\pi R_{17}^2 L_{17}$, μ/p_{17}^{th}, $(\gamma/R_{17})/B_{17}$, and p_{17}^{th}, respectively, where the subscript 17 refers to the mean value at the first generation of the respiratory zone. For simplicity, we assume that the air is an ideal gas at a fixed temperature.

(1) The applied stress σ_0 forces the volume of the intrapleural cavity to increase

$$\tilde{V}_{ip}(\tilde{t} + \Delta\tilde{t}) = \tilde{V}_{ip}(\tilde{t}) + \tilde{V}_{ip,0}[\varepsilon(\tilde{t} + \Delta\tilde{t}) - \varepsilon(\tilde{t})], \tag{3}$$

where $\varepsilon(t)$ is given by Eq. (1).

(2) Given a fixed amount of air within the intrapleural space, the expansion of the intrapleural cavity causes the pressure in the intrapleural cavity to concomitantly decrease

$$\tilde{p}_{ip}(\tilde{t} + \Delta\tilde{t}) = \frac{\tilde{p}_{ip}(\tilde{t})\tilde{V}_{ip}(\tilde{t})}{\tilde{V}_{ip}(\tilde{t} + \Delta\tilde{t})}. \tag{4}$$

(3) This decrease in intrapleural pressure transiently increases the transpulmonary pressure, which we estimate as

$$\tilde{p}_{tp}(\tilde{t} + \Delta\tilde{t}) \approx \tilde{p}_L(\tilde{t}) - \tilde{p}_{ip}(\tilde{t} + \Delta\tilde{t}). \tag{5}$$

We take $\tilde{p}_L$ to be a constant throughout the respiratory zone due to the low air flow resistance of the respiratory zone. In particular, we compare the flow resistance of air through the conducting zone or through the respiratory zone, $\Omega_C \approx \sum_{i=0}^{16}\left(\sum_{j=1}^{2^i}\Omega_{ij}^{-1}\right)^{-1}$ or $\Omega_R \approx \sum_{i=17}^{23}\left(\sum_{j=1}^{2^i}\Omega_{ij}^{-1}\right)^{-1}$, respectively, where the individual branch flow resistance $\Omega_{ij} = 8\mu_{air}L_i/\pi R_i^4$ is given by the Hagen-Poiseuille equation with an air viscosity $\mu_{air} \approx 18.5\ \mu$Pa s. Using measurements of L_i and R_i throughout the airways [56,59], we estimate $\Omega_C \approx 16.4$ and $\Omega_R \approx 0.2$ Pa s L^{-1}. Since $\Omega_R \ll \Omega_C$, we assume that the air flow resistance of the lungs is given by that of the conducting zone and the air pressure is constant throughout the respiratory zone.

(4) For each branch ij that is in contact with the open region of the lungs, if p_{tp} exceeds the threshold p_{ij}^{th}, this pressure difference across the branch wall forces it to open as given by Eq. (2),

$$\hat{V}_{ij}(\tilde{t} + \Delta\tilde{t}) = \hat{V}_{ij}(\tilde{t}) + \frac{\zeta\hat{R}_{ij}^3}{\hat{\Gamma}_{ij}}\left[\hat{p}_{tp}(\tilde{t} + \Delta\tilde{t}) - \hat{p}_{ij}^{th}\right]\Delta\tilde{t}. \tag{6}$$

(5) As branches open, the open volume of the lungs $V = V_C + \sum_{i=17}^{23}\sum_{j=1}^{2^i} V_{ij}$ increases, causing the pressure in the respiratory zone p_L to transiently decrease to an intermediate value $p_{L,int}$. In normal respiration, the lungs are an open system, and air in the lungs can be treated as incompressible so that its density does not vary with the pressure changes that arise during breathing due to inertial and viscous losses in the airways. However, in our discretized representation of the lungs for sufficiently small $\Delta\tilde{t}$, the lungs can be approximated to be a closed system at each intermediate time step: The timescale of volume changes in the lungs is much shorter than the characteristic air inflow timescale. Thus, assuming a constant V and a constant amount of air within the respiratory zone during this intermediate step, we estimate the intermediate pressure as

$$\tilde{p}_{L,int}(\tilde{t} + \Delta\tilde{t}) = \frac{\tilde{p}_L(\tilde{t})\tilde{V}_L(\tilde{t})}{\tilde{V}_L(\tilde{t} + \Delta\tilde{t})}. \tag{7}$$

(6) This decrease in pressure draws air into the lungs from the atmosphere with a volumetric flow rate q, driven by the pressure difference $\Delta p_{int} \equiv p_0 - p_{L,int}$. To evaluate this flow rate, we first consider the limit of $\Omega_C \to 0$; in this case, the pressure difference is fully equilibrated at each time step, and conservation of the amount of air exchanged yields $q = \frac{\Delta p_{int} V}{p_0 \Delta t} = \frac{\Delta p_{int}}{\Omega_0}$, where $\Omega_0 \equiv p_0\Delta t/V$ is an intrinsic resistance that reflects the discrete time formulation of the simulation. For the case of $\Omega_C > 0$, we then modify this expression to also incorporate Ω_C,

$$\tilde{q}(\tilde{t} + \Delta\tilde{t}) = \frac{\Delta\tilde{p}_{int}(\tilde{t} + \Delta\tilde{t})}{\tilde{\Omega}_0(\tilde{t} + \Delta\tilde{t}) + \tilde{\Omega}_C}. \tag{8}$$

(7) Because $\Omega_C > 0$, this air flow does not fully equilibrate the pressure difference Δp_{int}. Instead, the pressure in the respiratory zone at the end of the time step is given by

$$\tilde{p}_L(\tilde{t} + \Delta\tilde{t}) = \tilde{p}_{L,int}(\tilde{t} + \Delta\tilde{t}) + \frac{\tilde{q}(\tilde{t} + \Delta\tilde{t})\Delta\tilde{t}}{\tilde{V}_L(\tilde{t} + \Delta\tilde{t})}. \tag{9}$$

For each simulation presented in the main text, we iteratively solve Eqs. (3)–(9) over successive time steps separated by $\Delta\tilde{t} = 10^{-3}$ up to $\tilde{t} = 20$. We obtain identical results with even finer discretization as shown for the case of $\Delta\tilde{t} = 10^{-4}$ in Fig. 7, validating the assumptions made in Steps 5 and 6 above. This iterative solving is performed using a C++ framework that explicitly considers a given lung network structure described by the input morphological parameters $\{R_{ij}, L_{ij}, T_{ij}, V_{ip,0}\}$ and the biomechanical parameters $\{\mu, \gamma, E, \nu, \sigma_0, K_{ip}, p_{ip,0}\}$. This framework is split into a layer of virtual classes that treat memory management, multithreading, and provide the basic functions to create a branched network; each simulation is then derived from these virtual base classes with data structures defining the specific parameters that are input into the model. This scheme, thus, enables us to determine the full evolution of the pressures $\{\tilde{p}_{ip}, \tilde{p}_{tp}, \tilde{p}_L\}$, the volumes $\{\tilde{V}_{ip}, \hat{V}_{ij}, \tilde{V}\}$ and the flow rate $\tilde{q}$ over time $\tilde{t}$.

The code necessary to reproduce the results reported here and to further explore the dynamic network model is available in a Github repository [113].

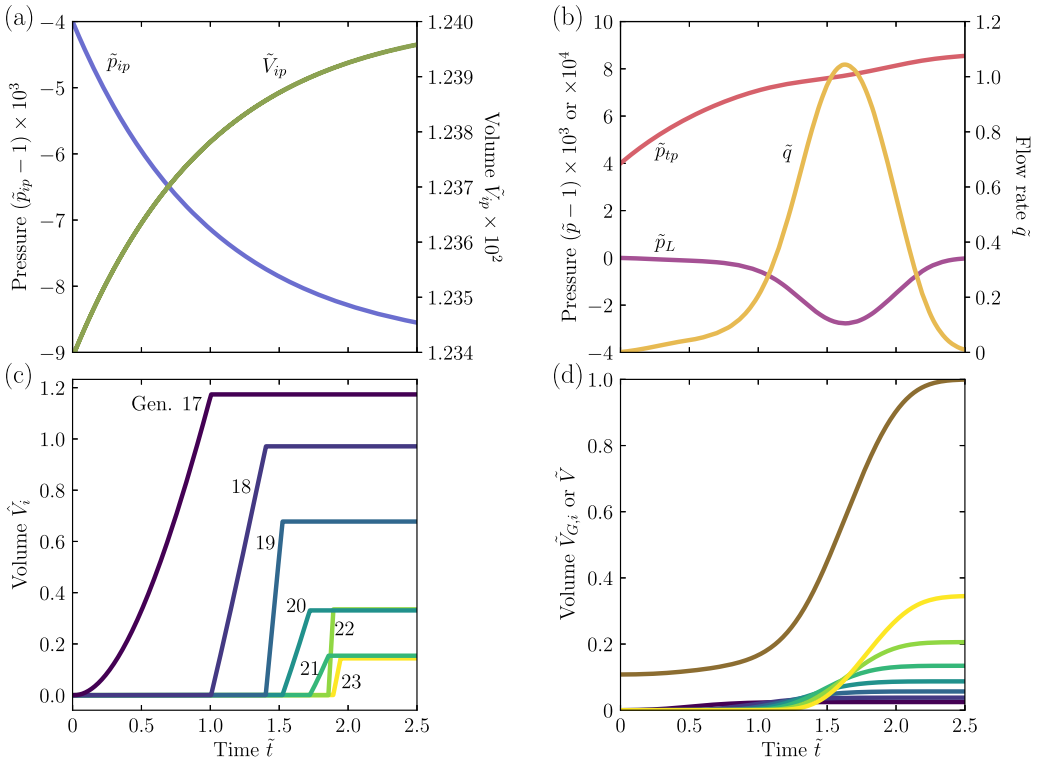

FIG. 7. Simulation results do not change with finer discretization. Plots show the simulated evolution of lung pressures and volumes just as in Fig. 2 but with a smaller time-step $\Delta\tilde{t} = 10^{-4}$; results are indistinguishable from those presented in the main text with a large time-step $\Delta\tilde{t} = 10^{-3}$.

ACKNOWLEDGMENTS

This work was supported by startup funds from Princeton University as well as partial support from the Keller Center REACH Program for F.K. It is a pleasure to acknowledge N. Ji and A. Sudhakar for their work on a preliminary version of the network model at the inception of this project.

All authors helped to design simulations; S.S.D. and J.-F.L. designed and performed the theoretical analysis; F.K. performed all simulations; J.-F.L., F.K., and S.S.D. analyzed the data; J.-F.L., F.K., and S.S.D. discussed the results and implications and wrote the paper; S.S.D. designed and supervised the overall project.

[1] Z. Xu, L. Shi, Y. Wang, J. Zhang, L. Huang, C. Zhang, S. Liu, P. Zhao, H. Liu, L. Zhu *et al.*, Pathological findings of COVID-19 associated with acute respiratory distress syndrome, Lancet Respir. Med. **8**, 420 (2020).

[2] C. Sohrabi, Z. Alsafi, N. O'Neill, M. Khan, A. Kerwan, A. Al-Jabir, C. Iosifidis, and R. Agha, World health organization declares global emergency: A review of the 2019 novel coronavirus (COVID-19), Int. J. Surgery **76**, 71 (2020).

[3] C. Qin, L. Zhou, Z. Hu, S. Zhang, S. Yang, Y. Tao, C. Xie, K. Ma, K. Shang, W. Wang, *et al.*, Dysregulation of immune response in patients with COVID-19 in Wuhan, China, Clin. Infect. Dis. **71**, 762 (2020).

[4] N. Poyiadji, G. Shahin, D. Noujaim, M. Stone, S. Patel, and B. Griffith, COVID-19–associated acute hemorrhagic necrotizing encephalopathy: CT and MRI features, Radiology **296**, E119 (2020).

[5] W.-H. Chen, U. Strych, P. J. Hotez, and M. E. Bottazzi, The SARS-CoV-2 vaccine pipeline: An overview, Curr. Trop. Med. Rep. **7**, 61 (2020).

[6] X.-W. Xu, X.-X. Wu, X.-G. Jiang, K.-J. Xu, L.-J. Ying, C.-L. Ma, S.-B. Li, H.-Y. Wang, S. Zhang, H.-N. Gao *et al.*, Clinical findings in a group of patients infected with the 2019 novel coronavirus (SARS-Cov-2) outside of Wuhan, China: retrospective case series, BMJ **368**, m792 (2020).

[7] W.-R. Luo, H. Yu, J.-Z. Gou, X.-X. Li, Y. Sun, J.-X. Li, J.-X. He, and L. Liu, Histopathologic findings in the explant lungs of a patient with COVID-19 treated with bilateral orthotopic lung transplant, Transplantation **104**, e329 (2020).

[8] R. A. Polin, W. A. Carlo *et al.*, Surfactant replacement therapy for preterm and term neonates with respiratory distress, Pediatrics **133**, 156 (2014).

[9] R. Mac Sweeney and D. F. McAuley, Acute respiratory distress syndrome, The Lancet **388**, 2416 (2016).

[10] B. T. Thompson, R. C. Chambers, and K. D. Liu, Acute respiratory distress syndrome, New England J. Med. **377**, 562 (2017).

[11] C. L. N. Oliveira, A. D. Araújo, J. H. T. Bates, J. S. Andrade Jr., and B. Suki, Entropy production and the pressure–volume curve of the lung, Front. Physiol. **7**, 73 (2016).

[12] M. Robinson and P. T. B. Bye, Mucociliary clearance in cystic fibrosis, Pediatric Pulmonology **33**, 293 (2002).

[13] P. A. Newhouse, F. White, J. H. Marks, and D. N. Homnick, The intrapulmonary percussive ventilator and flutter device compared to standard chest physiotherapy in patients with cystic fibrosis, Clin. Pediatr. **37**, 427 (1998).

[14] P. B. Davis and P. A. di Sant'Agnese, Assisted ventilation for patients with cystic fibrosis, Jama **239**, 1851 (1978).

[15] B. Fauroux, M. Boulé, F. Lofaso, F. Zérah, A. Clément, A. Harf, and D. Isabey, Chest physiotherapy in cystic fibrosis: improved tolerance with nasal pressure support ventilation, Pediatrics **103**, e32 (1999).

[16] N. G. McElvaney, R. C. Hubbard, P. Birrer, R. G. Crystal, M. S. Chernick, M. M. Frank, and D. B. Caplan, Aerosol α1-antitrypsin treatment for cystic fibrosis, The Lancet **337**, 392 (1991).

[17] M. Griese, P. Bufler, J. Teller, and D. Reinhardt, Nebulization of a bovine surfactant in cystic fibrosis: a pilot study, Eur. Respir. J. **10**, 1989 (1997).

[18] G. Devendra and R. G. Spragg, Lung surfactant in subacute pulmonary disease, Respir. Res. **3**, 11 (2002).

[19] H. Clark and K. Reid, The potential of recombinant surfactant protein d therapy to reduce inflammation in neonatal chronic lung disease, cystic fibrosis, and emphysema, Arch. Dis. Child. **88**, 981 (2003).

[20] M. Griese, P. Birrer, and A. Demirsoy, Pulmonary surfactant in cystic fibrosis, Eur. Respir. J. **10**, 1983 (1997).

[21] D. N. Homnick, F. White, and C. de Castro, Comparison of effects of an intrapulmonary percussive ventilator to standard aerosol and chest physiotherapy in treatment of cystic fibrosis, Pediatric Pulmonology **20**, 50 (1995).

[22] A. E. Holland, L. Denehy, G. Ntoumenopoulos, M. T. Naughton, and J. W. Wilson, Non-invasive ventilation assists chest physiotherapy in adults with acute exacerbations of cystic fibrosis, Thorax **58**, 880 (2003).

[23] M. E. Hodson, B. P. Madden, M. H. Steven, V. T. Tsang, and M. H. Yacoub, Non-invasive mechanical ventilation for cystic fibrosis patients–a potential bridge to transplantation, Eur. Respir. J. **4**, 524 (1991).

[24] D. K. Walters, G. W. Burgreen, D. M. Lavallee, D. S. Thompson, and R. L. Hester, Efficient, physiologically realistic lung airflow simulations, IEEE Trans. Biomed. Eng. **58**, 3016 (2011).

[25] B. Soni and S. Aliabadi, Large-scale CFD simulations of airflow and particle deposition in lung airway, Comput. Fluids **88**, 804 (2013).

[26] B. Ma and K. R. Lutchen, An anatomically based hybrid computational model of the human lung and its application to low frequency oscillatory mechanics, Ann. Biomed. Eng. **34**, 1691 (2006).

[27] W. A. Wall, L. Wiechert, A. Comerford, and S. Rausch, Towards a comprehensive computational model for the respiratory system, Int. J. Numer. Methods Biomed. Eng. **26**, 807 (2010).

[28] T. A. Lewis, Y.-S. Tzeng, E. L. McKinstry, A. C. Tooker, K. Hong, Y. Sun, J. Mansour, Z. Handler, and M. S. Albert, Quantification of airway diameters and 3D airway tree rendering from dynamic hyperpolarized 3He magnetic resonance imaging, Magn. Reson. Med. **53**, 474 (2005).

[29] N. Nowak, P. P. Kakade, and A. V. Annapragada, Computational fluid dynamics simulation of airflow and aerosol deposition in human lungs, Ann. Biomed. Eng. **31**, 374 (2003).

[30] J. Sznitman, S. Schmuki, R. Sutter, A. Tsuda, and T. Rösgen, CFD investigation of respiratory flows in a space-filling pulmonary acinus model, Modelling in Medicine and Biology VII, WIT Transactions on Biomedicine and Health **12**, 147 (2007).

[31] D. K. Walters and W. H. Luke, Computational fluid dynamics simulations of particle deposition in large-scale, multigenerational lung models, J. Biomech. Eng., **133**, 011003 (2011).

[32] D. K. Walters and W. H. Luke, A method for three-dimensional navier–stokes simulations of large-scale regions of the human lung airway, J. Fluids Eng., **132**, 051101 (2010).

[33] R. F. Kunz, D. C. Haworth, D. P. Porzio, and A. Kriete, Progress towards a medical image through CFD analysis toolkit for respiratory function assessment on a clinical time scale, in *2009 IEEE International Symposium on Biomedical Imaging: From Nano to Macro, Boston, 2009* (IEEE, Piscataway, NJ, 2009), pp. 382–385.

[34] R. K. Calay, J. Kurujareon, and A. Erik Holdø, Numerical simulation of respiratory flow patterns within human lung, Respir. Physiol. Neurobiol. **130**, 201 (2002).

[35] M. Malve, S. Chandra, J. L. Lopez-Villalobos, E. A. Finol, A. Ginel, and M. Doblare, CFD analysis of the human airways under impedance-based boundary conditions: application to healthy, diseased and stented trachea, Comput. Methods Biomech. Biomed. Eng. **16**, 198 (2013).

[36] W. A. Wall and T. Rabczuk, Fluid–structure interaction in lower airways of CT-based lung geometries, Int. J. Numer. Methods Fluids **57**, 653 (2008).

[37] T. Gemci, V. Ponyavin, Y. Chen, H. Chen, and R. Collins, Computational model of airflow in upper 17 generations of human respiratory tract, J. Biomech. **41**, 2047 (2008).

[38] A. L. Hazel and M. Heil, Three-dimensional airway reopening: the steady propagation of a semi-infinite bubble into a buckled elastic tube, J. Fluid Mech. **478**, 47 (2003).

[39] M. Heil, A. L. Hazel, and J. A. Smith, The mechanics of airway closure, Respir. Physiol. Neurobiol. **163**, 214 (2008).

[40] J. B. Grotberg, Respiratory fluid mechanics, Phys. Fluids **23**, 021301 (2011).

[41] D. Halpern and J. B. Grotberg, Fluid-elastic instabilities of liquid-lined flexible tubes, J. Fluid Mech. **244**, 615 (1992).

[42] J. B. Grotberg, Pulmonary flow and transport phenomena, Annu. Rev. Fluid Mech. **26**, 529 (1994).

[43] J. B. Grotberg and O. E. Jensen, Biofluid mechanics in flexible tubes, Annu. Rev. Fluid Mech. **36**, 121 (2004).

[44] M. Heil and A. L. Hazel, Fluid-structure interaction in internal physiological flows, Annu. Rev. Fluid Mech. **43**, 141 (2011).

[45] D. P. Gaver, D. Halpern, O. E. Jensen, and J. B. Grotberg, The steady motion of a semi-infinite bubble through a flexible-walled channel, J. Fluid Mech. **319**, 25 (1996).

[46] A. L. Hazel and M. Heil, The influence of gravity on the steady propagation of a semi-infinite bubble into a flexible channel, Phys. Fluids **20**, 092109 (2008).

[47] A. Juel and A. Heap, The reopening of a collapsed fluid-filled elastic tube, J. Fluid Mech. **572**, 287 (2007).

[48] M. Heil, Airway closure: occluding liquid bridges in strongly buckled elastic tubes, J. Biomech. Eng. **121**, 487 (1999).

[49] A. L. Hazel and M. Heil, Surface-tension-induced buckling of liquid-lined elastic tubes: a model for pulmonary airway closure, Proc. R. Soc. London A **461**, 1847 (2005).

[50] M. Heil, Stokes flow in collapsible tubes: computation and experiment, J. Fluid Mech. **353**, 285 (1997).

[51] M. Heil and T. J. Pedley, Large post-buckling deformations of cylindrical shells conveying viscous flow, J. Fluid. Struct. **10**, 565 (1996).

[52] C. Wongviriyawong, T. Winkler, R. S. Harris, and J. G. Venegas, Dynamics of tidal volume and ventilation heterogeneity under pressure-controlled ventilation during bronchoconstriction: a simulation study, J. Appl. Physiol. **109**, 1211 (2010).

[53] A. Z. Politi, G. M. Donovan, M. H. Tawhai, M. J. Sanderson, A.-M. Lauzon, J. H. T. Bates, and J. Sneyd, A multiscale, spatially distributed model of asthmatic airway hyperresponsiveness, J. Theor. Biol. **266**, 614 (2010).

[54] G. M. Donovan, Inter-airway structural heterogeneity interacts with dynamic heterogeneity to determine lung function and flow patterns in both asthmatic and control simulated lungs, J. Theor. Biol. **435**, 98 (2017).

[55] P. S. Stewart and O. E. Jensen, Patterns of recruitment and injury in a heterogeneous airway network model, J. R. Soc., Interface **12**, 20150523 (2015).

[56] E. R. Weibel, *Morphometry of the Human Lung* (Springer-Verlag, Berlin, Heidelberg, 1963).

[57] K. Horsfield, G. Dart, D. E. Olson, G. F. Filley, and G. Cumming, Models of the human bronchial tree, J. Appl. Physiol. **31**, 207 (1971).

[58] G. Nucci, S. Tessarin, and C. Cobelli, A morphometric model of lung mechanics for time-domain analysis of alveolar pressures during mechanical ventilation, Ann. Biomed. Eng. **30**, 537 (2002).

[59] R. H. Habib, R. B. Chalker, B. Suki, and A. C. Jackson, Airway geometry and wall mechanical properties estimated from subglottal input impedance in humans, J. Appl. Physiol. **77**, 441 (1994).

[60] J.-Y. Wang, P. Mesquida, P. Pallai, C. J. Corrigan, and T. H. Lee, Dynamic properties of human bronchial airway tissues, arXiv:1111.5645.

[61] M. A. Lewis and M. R. Owen, The mechanics of lung tissue under high-frequency ventilation, SIAM J. Appl. Math. **61**, 1731 (2001).

[62] S. J. Lai-Fook, R. E. Hyatt, and J. R. Rodarte, Elastic constants of trapped lung parenchyma, J. Appl. Physiol. **44**, 853 (1978).

[63] S. Baconnais, R. Tirouvanziam, J.-M. Zahm, S. de Bentzmann, B. Péault, G. Balossier, and E. Puchelle, Ion composition and rheology of airway liquid from cystic fibrosis fetal tracheal xenografts, Am. J. Respir. Cell Mol. Biol. **20**, 605 (1999).

[64] E. Puchelle, J. M. Zahm, and C. Duvivier, Spinability of bronchial mucus. relationship with viscoelasticity and mucous transport properties, Biorheology **20**, 239 (1983).

[65] H. Matsui, V. E. Wagner, D. B. Hill, U. E. Schwab, T. D. Rogers, B. Button, R. M. Taylor, R. Superfine, M. Rubinstein, B. H. Iglewski *et al.*, A physical linkage between cystic fibrosis airway surface dehydration and pseudomonas aeruginosa biofilms, Proc. Natl. Acad. Sci. USA **103**, 18131 (2006).

[66] P. D. Hughes, M. I. Polkey, M. L. Harris, A. J. S. Coats, J. Moxham, and M. Green, Diaphragm strength in chronic heart failure, Am. J. Respir. Crit. Care Med. **160**, 529 (1999).

[67] J. Ker *et al.*, Respiratory muscle endurance in heart failure–the effect of clinical severity, Cardiovascular J. Africa **9**, 20 (1998).

[68] M. I. Polkey, D. Kyroussis, C.-H. Hamnegard, G. H. Mills, M. Green, and J. Moxham, Diaphragm strength in chronic obstructive pulmonary disease, Am. J. Respir. Crit. Care Med. **154**, 1310 (1996).

[69] G. S. Supinski, P. Westgate, and L. A. Callahan, Correlation of maximal inspiratory pressure to transdiaphragmatic twitch pressure in intensive care unit patients, Critical Care **20**, 77 (2016).

[70] H. P. D'Agostino and M. A. Edens, Physiology, pleural fluid, *StatPearls* (StatPearls, Treasure Island, FL, 2019).

[71] R. V. Christie and C. A. McIntosh, The measurement of the intrapleural pressure in man and its significance, J. Clin. Invest. **13**, 279 (1934).

[72] M. Geiser, S. Schurch, and P. Gehr, Influence of surface chemistry and topography of particles on their immersion into the lung's surface-lining layer, J. Appl. Physiol. **94**, 1793 (2003).

[73] C. Alonso, A. Waring, and J. A. Zasadzinski, Keeping lung surfactant where it belongs: Protein regulation of two-dimensional viscosity, Biophys. J. **89**, 266 (2005).

[74] L. E. Fix, J. Khoury, R. R. Moores Jr., L. Linkous, M. Brandes, and Henry J. Rozycki, Theoretical open-loop model of respiratory mechanics in the extremely preterm infant, PloS One **13**, e0198425 (2018).

[75] X. Zhang and R. Z. Gan, Dynamic properties of human tympanic membrane based on frequency-temperature superposition, Ann. Biomed. Eng. **41**, 205 (2013).

[76] J. A. Blom, *Monitoring of Respiration and Circulation* (CRC, Boca Raton, FL 2003).

[77] B. Suki, A.-L. Barabási, Z. Hantos, F. Peták, and H. E. Stanley, Avalanches and power-law behavior in lung inflation, Nature (London) **368**, 615 (1994).

[78] B. Suki, A. M. Alencar, J. Tolnai, T. Asztalos, F. Peták, M. K. Sujeer, K. Patel, J. Patel, H. E. Stanley, and Z. Hantos, Size distribution of recruited alveolar volumes in airway reopening, J. Appl. Physiol. **89**, 2030 (2000).

[79] J. H. T. Bates and C. G. Irvin, Time dependence of recruitment and derecruitment in the lung: a theoretical model, J. Appl. Physiol. **93**, 705 (2002).

[80] W. Wang, J. Tang, and F. Wei, Updated understanding of the outbreak of 2019 novel coronavirus (2019-nCoV) in wuhan, china, J. Med. Virol. **92**, 441 (2020).

[81] V. Kim and G. J. Criner, Chronic bronchitis and chronic obstructive pulmonary disease, Am. J. Respir. Crit. Care Med. **187**, 228 (2013).

[82] M. J. Tobin, F. Laghi, and A. Jubran, Narrative review: ventilator-induced respiratory muscle weakness, Ann. Intern. Med. **153**, 240 (2010).

[83] W. J. Kozlowska and P. Aurora, Spirometry in the preschool age group, Paediatric Respiratory Rev. **6**, 267 (2005).

[84] S. K. Lai, Y.-Y. Wang, D. Wirtz, and J. Hanes, Micro-and macrorheology of mucus, Adv. Drug Delivery Rev. **61**, 86 (2009).

[85] B. K. Rubin, Mucus structure and properties in cystic fibrosis, Paediatric respiratory Rev. **8**, 4 (2007).

[86] J. M. Sturgess, A. J. Palfrey, and L. Reid, The viscosity of bronchial secretion, Clinical Sci. **38**, 145 (1970).

[87] Z. Ye, Y. Zhang, Y. Wang, Z. Huang, and B. Song, Chest CT manifestations of new coronavirus disease 2019 (COVID-19): A pictorial review, European Radiology, **30**, 4381 (2020).

[88] M. D. Bracco Lorenzo, COVID-19, Type II alveolar cells and surfactant, J. Med.–Clin. Res. Rev. **4**, 1 (2020).

[89] A. Günther, C. Ruppert, R. Schmidt, P. Markart, F. Grimminger, D. Walmrath, and W. Seeger, Surfactant alteration and replacement in acute respiratory distress syndrome, Respir. Res. **2**, 353 (2001).

[90] L. E. Gralinski and R. S. Baric, Molecular pathology of emerging coronavirus infections, J. Pathol. **235**, 185 (2015).

[91] Y. Yi, P. N. P. Lagniton, S. Ye, E. Li, and R.-H. Xu, COVID-19: what has been learned and to be learned about the novel coronavirus disease, Int. J. Biol. Sci. **16**, 1753 (2020).

[92] J. M. Hohlfeld, The role of surfactant in asthma, Respir. Res. **3**, 4 (2001).

[93] E. P. Ingenito, L. W. Tsai, A. Majumdar, and B. Suki, On the role of surface tension in the pathophysiology of emphysema, Am. J. Respir. Crit. Care Med. **171**, 300 (2005).

[94] A. M. Alencar, S. P. Arold, S. V. Buldyrev, A. Majumdar, D. Stamenović, H. E. Stanley, and B. Suki, Dynamic instabilities in the inflating lung, Nature (London) **417**, 809 (2002).

[95] H. D. Crane, Switching properties in bubbles, balloons, capillaries and alveoli, J. Biomech. **6**, 411 (1973).

[96] N. Limjunyawong, J. Fallica, M. R. Horton, and W. Mitzner, Measurement of the pressure-volume curve in mouse lungs, J. Vis Exp. **27**, 52376 (2015).

[97] H. A. W. M. Tiddens, S. H. Donaldson, M. Rosenfeld, and P. D. Paré, Cystic fibrosis lung disease starts in the small airways: can we treat it more effectively? Pediatric Pulmonology **45**, 107 (2010).

[98] G. M. Coates and M. S. Ersner, Occurrence of eosinophils in the mucous membrane of the maxillary sinus in asthmatic patients, Arch. Otolaryngol. **11**, 158 (1930).

[99] J. L. Wright and A. Churg, Advances in the pathology of COPD, Histopathology **49**, 1 (2006).

[100] B. Suki, R. Jesudason, S. Sato, H. Parameswaran, A. D. Araujo, A. Majumdar, P. G. Allen, and E. Bartolák-Suki, Mechanical failure, stress redistribution, elastase activity and binding site availability on elastin during the progression of emphysema, Pulm. Pharmacol. Ther. **25**, 268 (2012).

[101] K. Ohnishi, M. Takagi, Y. Kurokawa, S. Satomi, and Y. T. Konttinen, Matrix metalloproteinase-mediated extracellular matrix protein degradation in human pulmonary emphysema, Laboratory investigation; a journal of technical methods and pathology **78**, 1077 (1998).

[102] J. de Ryk, J. Thiesse, E. Namati, and G. McLennan, Stress distribution in a three dimensional, geometric alveolar sac under normal and emphysematous conditions, Int. J. Chronic Obstruct. Pulm. Dis. **2**, 81 (2007).

[103] E. Puchelle, O. Bajolet, and M. Abély, Airway mucus in cystic fibrosis, Paediatric respiratory reviews **3**, 115 (2002).

[104] D. F. Rogers and P. J. Barnes, Treatment of airway mucus hypersecretion, Ann. Med. **38**, 116 (2006).

[105] G. Piatti, U. Ambrosetti, P. Santus, and L. Allegra, Effects of salmeterol on cilia and mucus in COPD and pneumonia patients, Pharmacol. Res. **51**, 165 (2005).

[106] T. Barreiro and I. Perillo, An approach to interpreting spirometry, Am. Fam. Physician **69**, 1107 (2004).

[107] W. M. Gold and L. L. Koth, Pulmonary function testing, *Murray and Nadel's Textbook of Respiratory Medicine* (Elsevier, Amsterdam, 2016).

[108] *The Gobal Impact of Respiratory Disease, Forum of International Respiratory Societies, Sheffield*, Second ed. (European Respiratory Society, Lausanne, Switzerland, 2017).

[109] A. Heap and A. Juel, Bubble transitions in strongly collapsed elastic tubes, J. Fluid Mech. **633**, 485 (2009).

[110] J. A. Moriarty and J. B. Grotberg, Flow-induced instabilities of a mucus–serous bilayer, J. Fluid Mech. **397**, 1 (1999).

[111] F. Romanò, H. Fujioka, M. Muradoglu, and J. B. Grotberg, Liquid plug formation in an airway closure model, Phys. Rev. Fluids **4**, 093103 (2019).

[112] B. Mauroy, P. Flaud, D. Pelca, C. Fausser, J. Merckx, and Barrett R. Mitchell, Toward the modeling of mucus draining from human lung: role of airways deformation on air-mucus interaction, Front. Physiol. **6**, 214 (2015).

[113] https://github.com/FelixKratz/LungFramework.